Burns & Trauma, 2025, **13**, tkaf028
https://doi.org/10.1093/burnst/tkaf028
Research Article

Three-dimensional composite aerogel scaffolds based on electrospun poly(lactic acid)/gelatin and silica-strontium oxide short fibers promote bone defect healing

Jie Cui[1,‡], Lixiang Zhang[2,‡], Muhammad Shafiq[3], Panpan Shang[4], Xiao Yu[1], Yangfan Ding[1], Pengfei Cai[5], JiaHui Song[1], Binbin Sun[1], Mohamed EL-Newehy[6], Meera Moydeen Abdulhameed[6], Stachewicz Urszula[7], Xingping Zhou[1,*], Yuan Xu[2,*], Xiumei Mo[1,4,*]

[1]State Key Laboratory for Modification of Chemical Fibers and Polymer Materials, Shanghai Engineering Research Center of Nano-Biomaterials and Regenerative Medicine, College of Biological Science and Medical Engineering, No. 2999 North Renmin Road, Songjiang District, Donghua University, Shanghai 201620, P.R. China
[2]Department of Orthopaedics, Xinqiao Hospital, Army Medical University, No. 183, Xinqiao Street, Shapingba District, Chongqing 400037, P. R. China
[3]Innovation Center of NanoMedicine (iCONM), Kawasaki Institute of Industrial Promotion, Kawasaki-ku, Kawasaki 210-0821, Japan
[4]Institute of Biomaterials and Biomedicine, School of Food and Pharmacy, Shanghai Zhongqiao Vocational and Technical University, Shanghai 201514, P.R. China
[5]G.E.R.N. Research Center for Tissue Replacement, Regeneration & Neogenesis, Department of Orthopedics and Trauma Surgery, Faculty of Medicine, Medical Center-Albert-Ludwigs-University of Freiburg, 79085 Freiburg in Breisgau, Germany
[6]Department of Chemistry, College of Science, King Saud University, P.O. Box 2455, Riyadh 11451, Saudi Arabia
[7]AGH University of Krakow, college of Materials, Poland

*Corresponding authors. Xiumei Mo (xmm@dhu.edu.cn); Yuan Xu (15123161526@163.com); Xingping Zhou (xpzhou@dhu.edu.cn)

‡Jie Cui and Lixiang Zhang contributed equally to this work.

Abstract

Background: Bone defect regeneration is a dynamic healing process that relies on the body's innate repair mechanisms, yet natural healing capacity remains limited. To address this challenge, advanced biomaterials combining bioactive inorganic components with biocompatible polymers have emerged as a promising strategy to enhance osteogenesis and angiogenesis.

Methods: In this study, a novel three-dimensional composite scaffold material was successfully fabricated using a combined electrospinning-freeze drying technique. The scaffold incorporates flexible silicon dioxide-strontium oxide (SiO_2-SrO) nanofibers as functional components, which are physically blended with a poly(lactic acid)/gelatin (PG) fibrous matrix to achieve composite construction.

Result: The fabricated scaffolds exhibited an optimal well-ordered porous structure, excellent biocompatibility, and sustained release of therapeutic ions (Si^{4+} and Sr^{2+}). Notably, they significantly upregulated osteogenic gene expression and enhanced angiogenic potential as demonstrated by improved tubulogenesis in HUVEC cultures. In vivo evaluation using a rat calvarial defect model confirmed their superior bone regeneration capability through simultaneous promotion of osteogenesis and angiogenesis.

Conclusion: Leveraging the synergistic effects of SiO_2.SrO nanofibers and PG polymers, this study presents a multifunctional scaffold capable of promoting bone regeneration through dual osteogenic and angiogenic stimulation. Our findings highlight the potential of this composite system not only for bone tissue engineering but also for broader biomedical applications.

Received: December 10, 2024. **Revised:** March 26, 2025. **Accepted:** April 21, 2025

Graphical Abstract

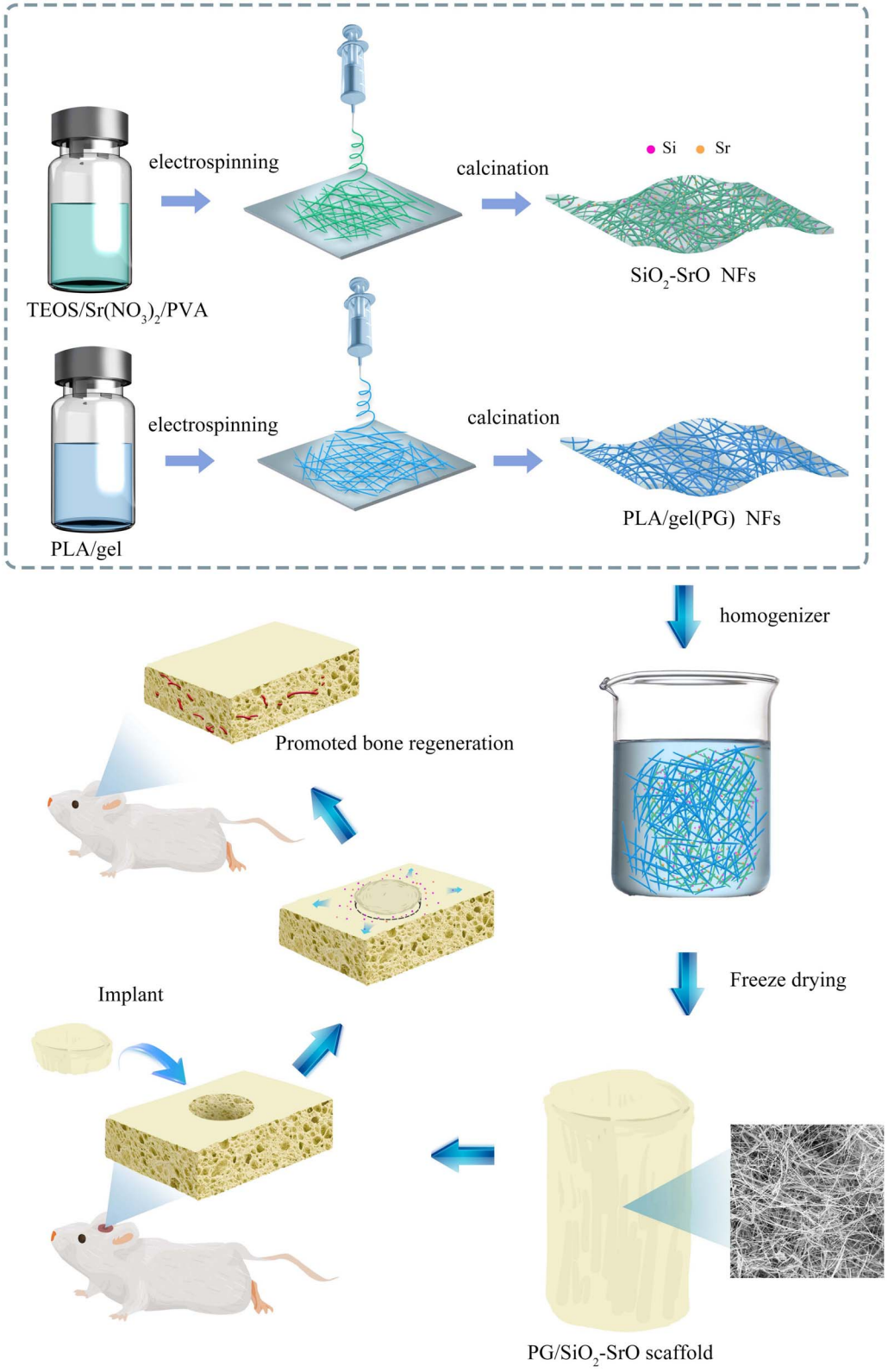

Keywords: Inorganic nanofiber; Composite scaffold; Calvarial repair; Electrospinning; Tissue engineering; Bone tissue engineering

Background

Bones play an important role in maintaining complete life functions as the body's internal support system, maintaining motor and hematopoietic functions, as well as protecting internal organs and the nervous system [1]. According to research, annual global bone graft surgeries exceed 2 million cases, the second most frequent transplantation following blood transfusion [2]. In addition to the most commonly used autologous or allogeneic bone substitutes, inorganic or bio-organic-based bone substitutes are also widely used for fracture repair [3]. Bone's structure is hierarchically organized, with type I collagen (COL1) providing organic flexibility and hydroxyapatite (HA) nanocrystals contributing mineral rigidity [4]. Organic–inorganic composite materials exhibit distinctive structural and biochemical characteristics, that are reminiscent of naturally occurring hybrid systems. In the presence of an extensive damage to the bone, the regeneration process of the resulting bone may be impaired due to an inability of the injury microenvironment to create a new vascular network to ensure oxygen permeation and nutrient delivery. Different types of inorganic nanomaterials (NMs) are being extensively used to promote bone tissue regeneration via enhanced osteogenesis and angiogenesis. Inorganic NMs, such as bioactive ceramics (e.g. HA, tricalcium phosphate, etc.) are being widely used in the clinic due to their potential advantages, including osteo-inductivity and osteo-conductivity albeit their poor mechanical properties and fragility. Organic/inorganic hybrids based on natural/synthetic polymers and inorganic NMs may hold great promise to recapitulate biomechanical characteristics of natural bone extracellular matrix (ECM) as well as harness the potential advantage of each individual component of the scaffold to synergistically promote osteogenesis and angiogenesis.The integration of multiple inorganic NMs enables the combined therapeutic potential of distinct bioactive ions, such as silicon ions (Si^{4+}) and strontium (Sr^{2+}) ions. Artificial bone graft materials capable of providing prolonged and regulated delivery of bioactive ions (e.g. Si^{4+}, Sr^{2+}, etc.) may not only promote stem cell differentiation into osteogenic and angiogenic cells but they may also work as depots for the sustained and controlled release of drugs [1]. Consequently, the application of inorganic NMs capable of furnishing therapeutic ions is a cost-effective and an economical approach to promote bone tissue repair.

Calcium (Ca) is one of the basic elements in the body, which makes up the mineral composition of bone. Strontium has physical and chemical properties similar to Ca; therefore, Sr^{2+} act through Ca-sensitive receptors in bone tissue to increase the production of osteoprotegerin and inhibition of RANKL binding to RANK receptors by decreasing its transcript levels, and thus inhibits osteoclastogenesis [5]. On the other hand, strontium (Sr) promotes bone tissue repair by enhanced osteoblast activity and functional performance. Wnt signaling critically regulates mesenchymal stromal cells (MSCs) osteogenic differentiation in bone repair. [6, 7]. The Sr activates the classical Wnt pathway by suppressing sclerostin expression and therefore promotes osteoblast differentiation. Similarly, Si can stimulate osteoblast CoL I expression and mineralized deposition [8]. *In vitro* experiments have confirmed that Si is a key influencing factor in the formation of collagen-proteoglycan cross-linking, thereby enhancing bone strength and biomechanical performance [9]. Silicon ions (Si^{4+}) exhibit pleiotropic effects through promoting stem cell differentiation, facilitating intercellular communication, and inducing angiogenesis via VEGF/VEGFR2 and IGF1/IGF1R signaling cascades [10–12]. Biomaterials incorporating SiO_2 enhance osteogenic activity through improved cell adhesion and proliferation along with increase the production of bone-specific proteins [9]. Min et al. reported the effect of Si/Sr co-promotion of osteoblast activity and vascularization [13].

Aerogels are low-density and highly mesoporous materials prepared by the self-assembly of sol-gels or molecular precursors (organic or inorganic) followed by processing using various techniques (e.g. drying, supercritical carbon dioxide, thermal crosslinking, etc,) [14]. Aerogels exhibit high water absorption, an interconnected porous structure and good permeability, which can promote the attachment, proliferation and migration of osteoblasts and angiogenic cells. Aerogels serve as delivery platforms enabling prolonged and tunable growth factor release, therapeutics, and bioactive ions (e.g. Si^{2+}, Sr^{2+}, Ca^{2+}, etc.), which may help promote osteogenic differentiation and neovascularization for enhanced the efficiency of bone defect repair [15]. El-Wakil et al. fabricated risedronate-loaded 3D aerogel scaffold, which were composed of nanofibrillated cellulose. These scaffolds both effectively inhibit bone tissue degradation and significantly promote new bone formation [16].

The aim of this study was to manufacture organic–inorganic hybrid aerogel scaffolds capable of furnishing therapeutic ions, e.g. Si^{4+} and Sr^{2+}. Poly(lactic acid)/gelatin (PLA/Gel) and silica-strontium oxide (SiO_2-SrO) fibers with different content of Sr were individually prepared by electrospinning and then homogenized to obtain short nanofibers. Organic/inorganic hybrid aerogels were then developed by blending appropriate proportions of flexible SiO_2-SrO fibers and PLA/Gel fibers. We envision that these organic/inorganic hybrid aerogels may not only mimic key structural features of natural bone ECM, but they may also simultaneously promote osteogenesis and angiogenesis. We thoroughly structural characterization of the scaffold, such as surface morphology, microstructure, and mechanical strength. Moreover, we examined cytocompatibility, angiogenic ability, osteogenic activity, and osteogenic activity *in vitro*. Using rat calvarial defects as a research platform, we not only evaluated the macroscopic repair effect of the scaffolds, but also analyzed the expression of relevant osteogenic markers by immunohistochemistry [17].

Methods

Manufacturing of electrospun nanofibrous membranes

PLA and Gel were dissolved in hexafluoroisopropanol (PLA:Gel = 1:5, w/w, %) to obtain 11% (w/v) solution. The parameters of electrostatic spinning were voltage 12 kV, propulsion pump speed 1 ml/hour, and reception distance 15 cm to prepare nanofiber membranes.

To prepare SiO_2-SrO fibers, varying content of Sr nitrate (e.g. 0.1, 0.2, 0.3%, etc.) were dissolved in TEOS/H_3PO_4/H_2O (10:0.07:10, v/v) solution and stirred for 10 h to obtain SiO_2-SrO sol. PVA was dissolved in deionized water at a mass ratio of 1:9. Subsequently, SiO_2-SrO sol and PVA solution were mixed at a 1:1 weight ratio and stirred for 5 h at 15°C. SiO_2-SrO fibers with varying content of Sr were prepared by electrospinning to obtain SiO_2-SrO-1 NF, SiO_2-SrO-2 NF, and SiO_2-SrO-3 NF with electrospinning

parameters as follows: applied voltage, 20 kV, flow rate, 1 ml/h, and spinner-to-collector distance, 15 cm. High-temperature heat treatment of fibers in a muffle furnace (800°C/2 h).

Fabrication and characterization of PG/SiO_2-SrO scaffolds

Preparation of PG/SiO_2-SrO scaffolds

PLA/Gel and silicon oxide/silica (SiO_2-SrO) fibers were cut into 1 cm × 1 cm sizes for the preparation of organic/inorganic hybrid aerogels. About 2.5 g of fibers with or without SiO_2-SrO fibers were mixed with 100 ml of tert-butanol and The in order to obtain a homogeneous nanofiber dispersion, the mixture was stirred at 10000 rpm for 30 minutes using a high-speed mixer (IKA T18, Germany). The mass ratio between PLLA/Gel fibers and SiO_2-SrO fibers was 6:4 (w/w) [18]. The blended solution was transferred into a 96-well plate and frozen at −80°C for 12 h, followed by lyophilization (FreeZone® 2.5 L, LABCONCO, USA) over 72 h to produce uncrosslinked 3D aerogel scaffolds. Scaffolds were thermally crosslinked at 190°C for up to 2 h in a muffle furnace (FO311C, YAMATO, Japan). The composite scaffolds prepared from SiO_2-SrO nanofibrous membranes with Sr content of 0.1%, 0.2%, and 0.3% were named as PG/SiO_2-SrO-1, PG/SiO_2-SrO-2, and PG/SiO_2-SrO-3, respectively. The composite scaffolds were cut into 1 mm thick slices and observed under a scanning electron microscope.

Structural elucidation and physico-chemical properties of scaffolds

The composite scaffolds were physically characterized as follows: scanning electron microscopy (SEM), energy dispersive spectroscopy, X-ray diffraction (XRD), Fourier transform infrared spectroscopy (FTIR), water contact angle test, inductively coupled plasma emission spectrometry for the detection of Si^{4+} and Sr^{2+} release, and thermogravimetric analysis (TGA), mechanical tests, and *in vitro* degradation tests (n = 3). *In vitro* degradation tests (n = 3). See the Supplementary Materials section for information on the operation of the test method.

In vitro biocompatibility of scaffolds

The study utilized three cell types: MC3T3-E1 pre-osteoblasts and human umbilical vein endothelial cells (HUVECs) from the Chinese Academy of Sciences Cell Bank, along with rBMSCs isolated from two-week-old Sprague–Dawley rats (supplied by Shanghai Jieshijie Laboratory Animal Co.). All cell lines were maintained under standard culture conditions (37°C, 5% CO2) with medium renewal every 48 hours.

To assess scaffold biocompatibility, four material groups (PG, PG/SiO_2-SrO-1, PG/SiO_2-SrO-2, and PG/SiO_2-SrO-3) were evaluated through multiple cellular assays (n = 3) including cell inoculation, cell proliferation, cell migration, and angiogenic potential (tube formation).

In vitro osteogenic activity of scaffolds

In order to evaluate the osteogenic differentiation potential of rBMSCs, alkaline phosphatase (ALP) activity assay and alizarin red S (ARS) staining were used to quantify the degree of early osteogenic differentiation and the formation of late Ca nodules, respectively. The levels of COL1, osteocalcin (OCN), osteoblast protein (OPN) and runt-related transcription factor 2 (RUNX2) were also assessed by real-time quantitative PCR (RT-qPCR). See the Supplementary Materials section for information on the operation of the test method.

Animal experiments

The animal study protocol was approved by the Institutional Animal Care and Use Committee of Army Medical University (Approval No. AMUWEC20256048). To discern the performance of the aerogel scaffolds to induce bone production *in vivo*, they were implanted into in a 5-mm-sized calvarial defects in a rat model. Inhalation anesthesia was administered to 8-week-old male Sprague–Dawley rats prior to procedures. Following anesthesia induction, a 2 cm scalp incision exposed the calvarial. After periosteal removal, 5 mm bilateral calvarial defects were drilled. Sterilized scaffolds (PG and PG/SiO_2-SrO-2), pre-cut into 1 mm thick disks, were then implanted into the defect sites. Animals were sacrificed at predetermined intervals (4, 8, and 12 weeks) post-implantation, with four specimens per group at each time point, and calvarial tissues were harvested and fixed in 4% paraformaldehyde. Tissue samples were scanned and examined using Micro-CT. After micro-CT scanning, bone specimens were decalcified, sectioned, and stained with hematoxylin & eosin (H&E) and Masson's trichrome for histological analysis. The thickness of the slices was 4 μm.

Statistical analyses

The experimental data were expressed as mean ± standard deviation (mean ± SD), and one-way ANOVA (one-way ANOVA) was used for between-group comparisons, and Tukey's method was chosen for post hoc tests. $^{*}P < .05$, $^{**}P < .01$, $^{***}P < .001$.

Results

Characterization properties of PG/SiO_2-SrO composite aerogel scaffolds

PLA/Gel and SiO_2-SrO fibers were fabricated using electrospinning. The SiO_2-SrO fibers were soft and foldable without a distinct rupture of the fibers. SEM analysis showed that the surface of SiO_2-SrO fibers showed continuous and homogeneous morphological features (Figure S1, Supporting Information). Energy-dispersive X-ray spectroscopy (EDX) exhibited uniform distribution of silicon (Si) and Sr elements in membranes (Figure S2, Supporting Information). PLA/Gel and SiO_2-SrO fibers were blended at an appropriate mixing ratio and freeze-dried to obtain organic/inorganic hybrid aerogels (Figure 1a). The composite scaffolds were cut into 1-mm-thick slices and observed with SEM, Unlike PLA/Gel aerogel scaffolds (PG), which exhibited mesopores and a compact sheet-like structure, organic/inorganic hybrid aerogels composed of both PLA/Gel and SiO_2-SrO fibers (PG/SiO_2-SrO) manifested porous structure as well as a stacking of short fibers (Figure 1b). EDX mapping showed homogenous distribution of Si and Sr elements in PG/SiO_2-SrO aerogels, this demonstrates the successful integration of SiO_2-SrO fibers into aerogels (Figure 1c).

FTIR spectra of PG/SiO_2-SrO-1, PG/SiO_2-SrO-2, and PG/SiO_2-SrO-3 exhibited a characteristic peak at 802 cm^{-1}, which was ascribed to the siloxane linkage (Si-O-Si) of the SiO_2. The bands at 1633 and 1540 cm^{-1} correspond to amide I and amide II bonds, respectively, generated upon Gel heat treatment [18], The 1751 cm^{-1} band corresponds to the PLA

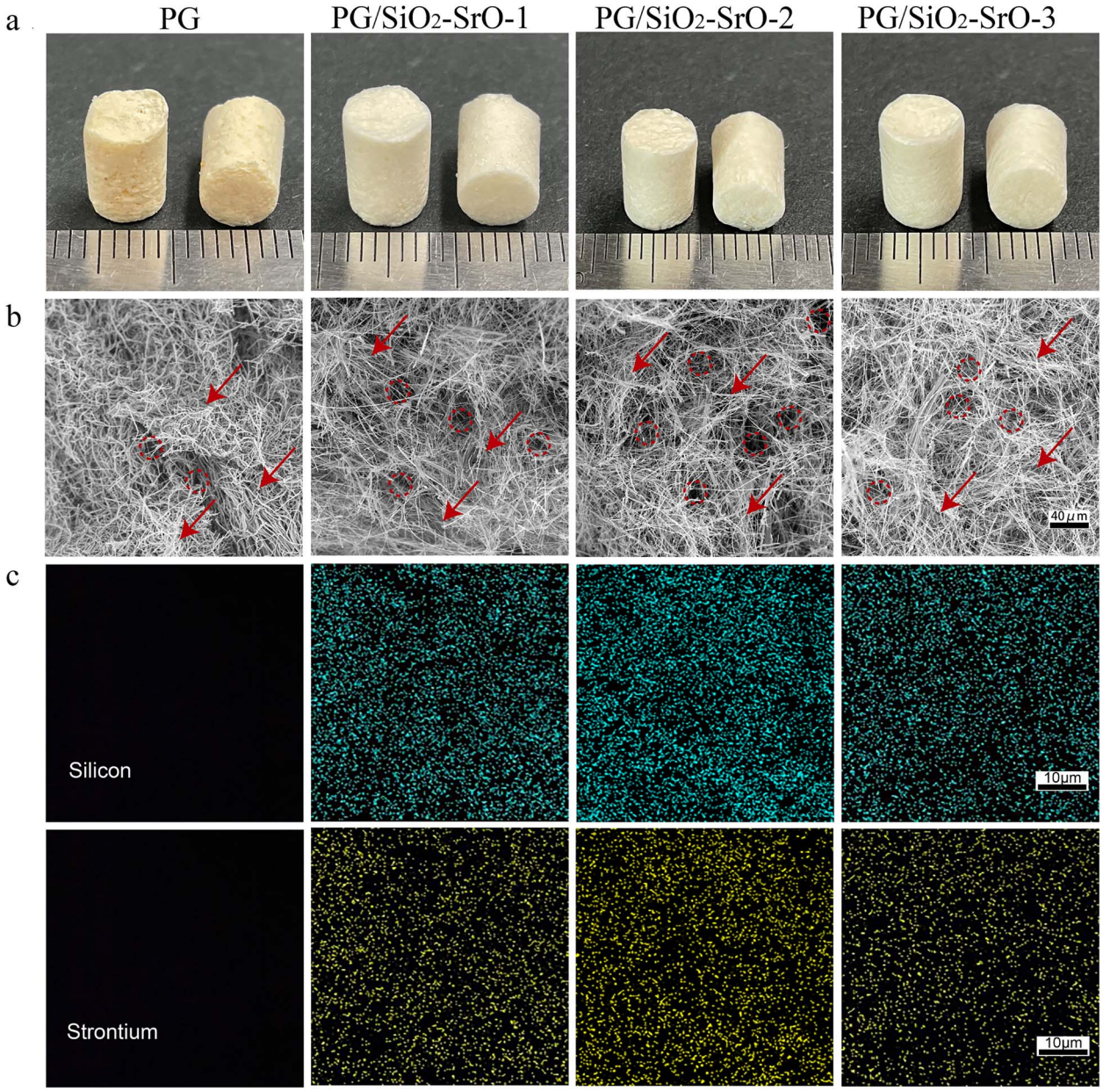

Figure 1. Morphological analysis of composite aerogel scaffolds. (**a**) Optical photographs and (**b**) SEM micrographs of scaffolds. Circles indicate pores among fibres, while arrows indicate the degree of fiber stacking in the scaffold. (**c**) EDX analysis showing homogenous distribution of Si and Sr in aerogel scaffolds. Scale bars = 40 μm (b) and 10 μm (c)

carbonyl (C=O) stretching vibration (Figure 2a) [19]. XRD spectra of scaffolds did not exhibit additional diffraction peaks, which is indicative of their amorphous structure (Figure 2b). Thermogravimetric analysis (TGA) showed an increase in the mass loss with an increase in the temperature (Figure 2c). As can be seen from TGA thermograms, rate of mass loss was slower in the PG/SiO_2-SrO groups than that of the PG, which is suggest of the higher thermal stability of aerogel scaffolds due in part to the incorporation of SiO_2-SrO fibers into scaffolds. As the temperature was increased to 800°C, the residual mass of PG group was 18.28%, while 50.33%, 49.55%, and 50.51%, for PG/SiO_2-SrO-1, PG/SiO_2-SrO-2 and PG/SiO_2-SrO-3 scaffolds, respectively. Differential scanning calorimetry (DSC) curves further showed the higher thermal stability of G/SiO_2-SrO scaffolds than that of the PG scaffolds (Figure 2d). Water contact angle test of the PG was $131.08 \pm 3.54°$, while $122.68 \pm 6.22°$, $100.60 \pm 14.58°$, and $98.55 \pm 14.86°$ for PG/SiO_2-SrO-1, PG/SiO_2-SrO-2, and PG/SiO_2-SrO-3 scaffolds, respectively. While carboxylic groups (-COOH) and amino (-NH_2) groups of Gel can form amide bonds after thermal crosslinking and reduce the hydrophilicity of the scaffolds, composite scaffolds exhibited better hydrophilicity, which is ascribed to the incorporation of flexible SiO_2-SrO fibers. Which made the PG/SiO_2-SrO scaffolds outperform the PG scaffolds in terms of hydrophilicity (Figure 2e).

The degradation of PG as well as composite scaffolds was ascertained *in vitro* for up to 8 weeks. The PG group lost ~50% of its mass over a period of 8 weeks. In contrast, composite scaffolds exhibited slower degradation than that of

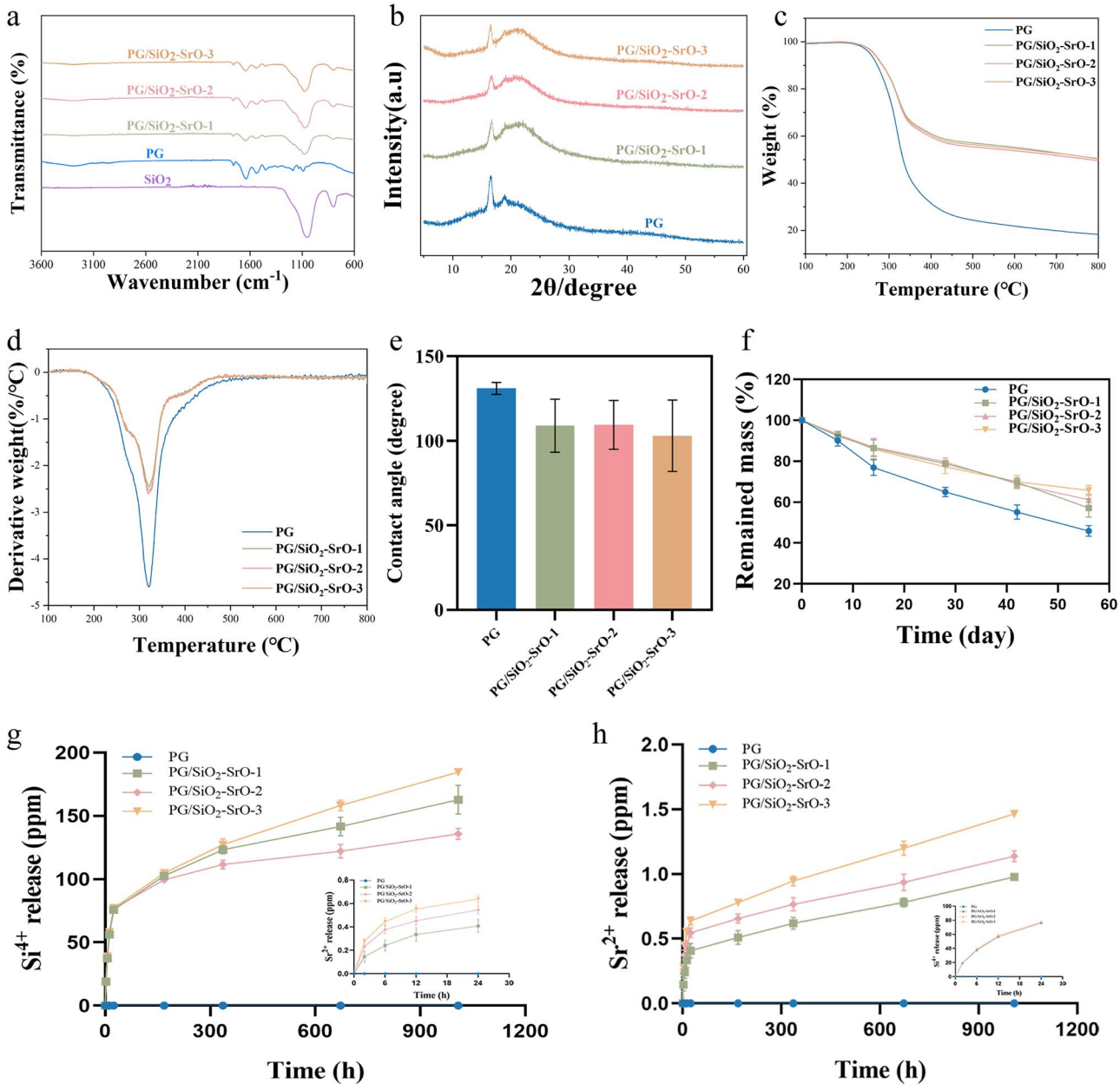

Figure 2. Physical and chemical properties of scaffolds. (**a**) FTIR spectra, (**b**) X-ray Diffraction (XRD) patterns, (**c**, **d**) thermograms, (**e**) Water Contact Angle (WCA), n = 3 (**f**) degradation in vitro, n = 3 and (G-H) release kinetics of silicon ions (Si^{4+}) and strontium ions (Sr^{2+}). n = 3

the PG group albeit similar residual weight after degradation *in vitro* (Figure 2f). The release kinetics of Si^{4+} and Sr^{2+} was further monitored for up to 45 days *in vitro* (Figure 2g-h). The PG/SiO_2-SrO-3 scaffolds exhibited higher content of released Sr^{2+}.

The representative stress–strain curves showed that each scaffold conformed to the basic law of Hooke's law during the initial compression process (Figure 3a). Maximum compressive strength of the PG, PG/SiO_2-SrO-1, PG/SiO_2-SrO-2, and PG/SiO_2-SrO-3 scaffolds was 631.4 ± 50.1 kPa, 909.3 ± 51.7 kPa, 969.1 ± 53.9 kPa, and 982.3 ± 59.0 kPa, respectively, under dry condition (Figure 3b). The PG/SiO_2-SrO scaffolds exhibited significantly higher compressive strength and compressive moduli than that of the PG albeit an insignificant difference among composite scaffold groups (Figure 3c). The values for the maximum compressive stress at 90% compressive strain were found to be 20.5 ± 3.3 N, 29.2 ± 1.1 N, 29.7 ± 1.6 N and 30.6 ± 0.4 N for PG, PG/SiO_2-SrO-1, PG/SiO_2-SrO-2, and PG/SiO_2-SrO-3 aerogel scaffolds, respectively (Figure 3d). While in the dry state, PG scaffolds underwent irreversible plastic deformation after compression, PG/SiO_2-SrO scaffolds were still able to maintain a certain degree of resilience.

While morphological analysis of PG scaffolds after compression manifested the compaction of the fibers and a denser stacking, PG/SiO_2-SrO scaffolds exhibited loose and porous fibrous (Figure 3e). The change in mechanical properties of the stent material after 1, 20 and 50 cycles of compression was tested by applying a 60% compressive strain to the stent material in an aqueous media environment. (Figure 3f-h). After 60% strain cyclic compression, the PG/SiO_2-SrO scaffold recovered its initial height (Figure 3i). Supplementary

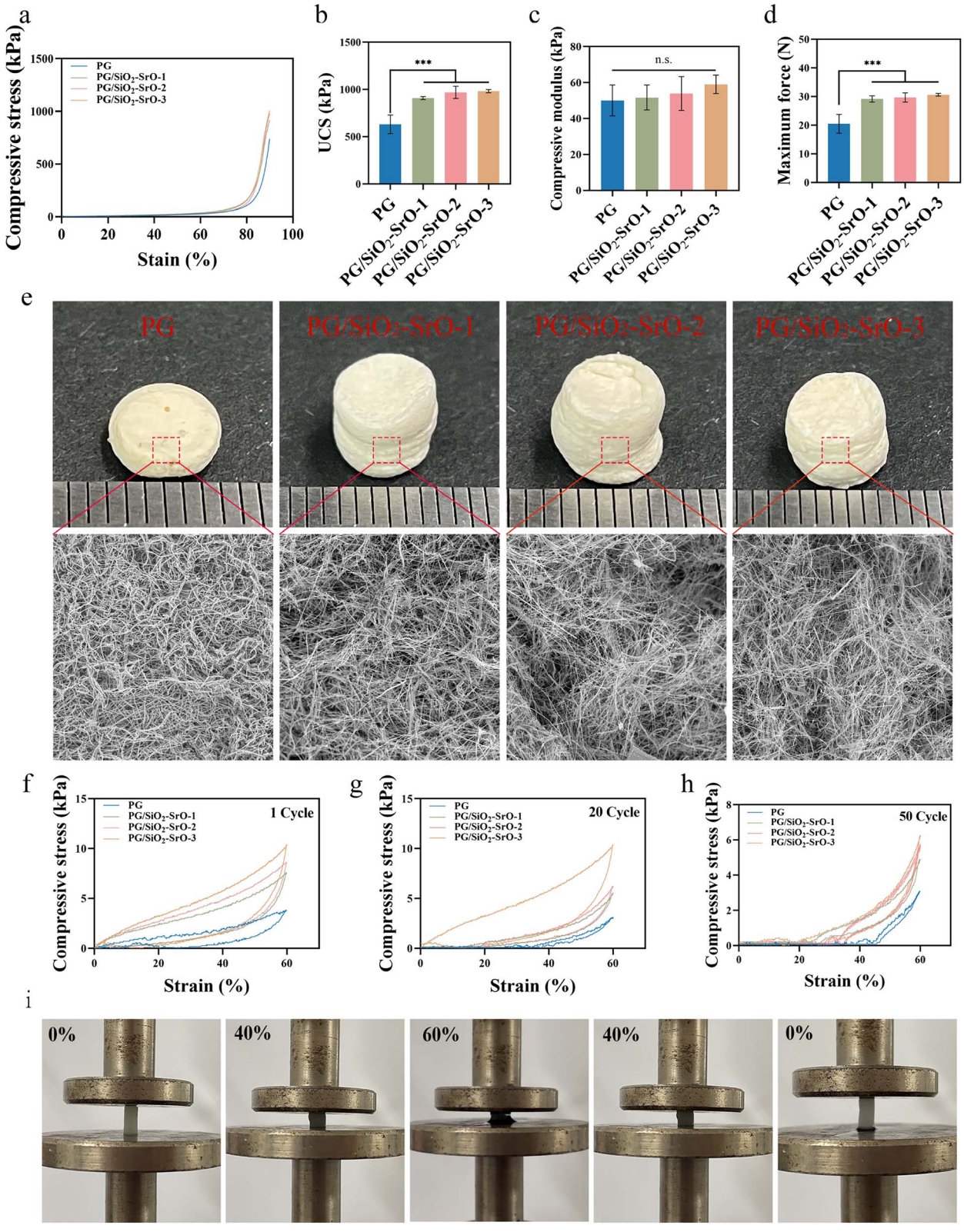

Figure 3. Compressive mechanical behavior of different types of scaffolds. (**a**) Representative compressive stress-strain curve. (**b**) Uniaxial Compressive Strength (UCS). n = 3. (**c**) Compression moduli of scaffolds (n = 3). (**d**) Maximum force (n = 3). (**e**) Morphological analysis of scaffolds compressed under dry conditions. (**f**-**h**) Compression cycles of various scaffolds in wet condition, 1 compression cycle, 20 compression cycles and 50 compression cycles. (**i**) Macrostructural changes during compression and shape recovery in an aqueous medium. $^{*}p < 0.05$, $^{**}p < 0.01$, $^{***}p < 0.001$

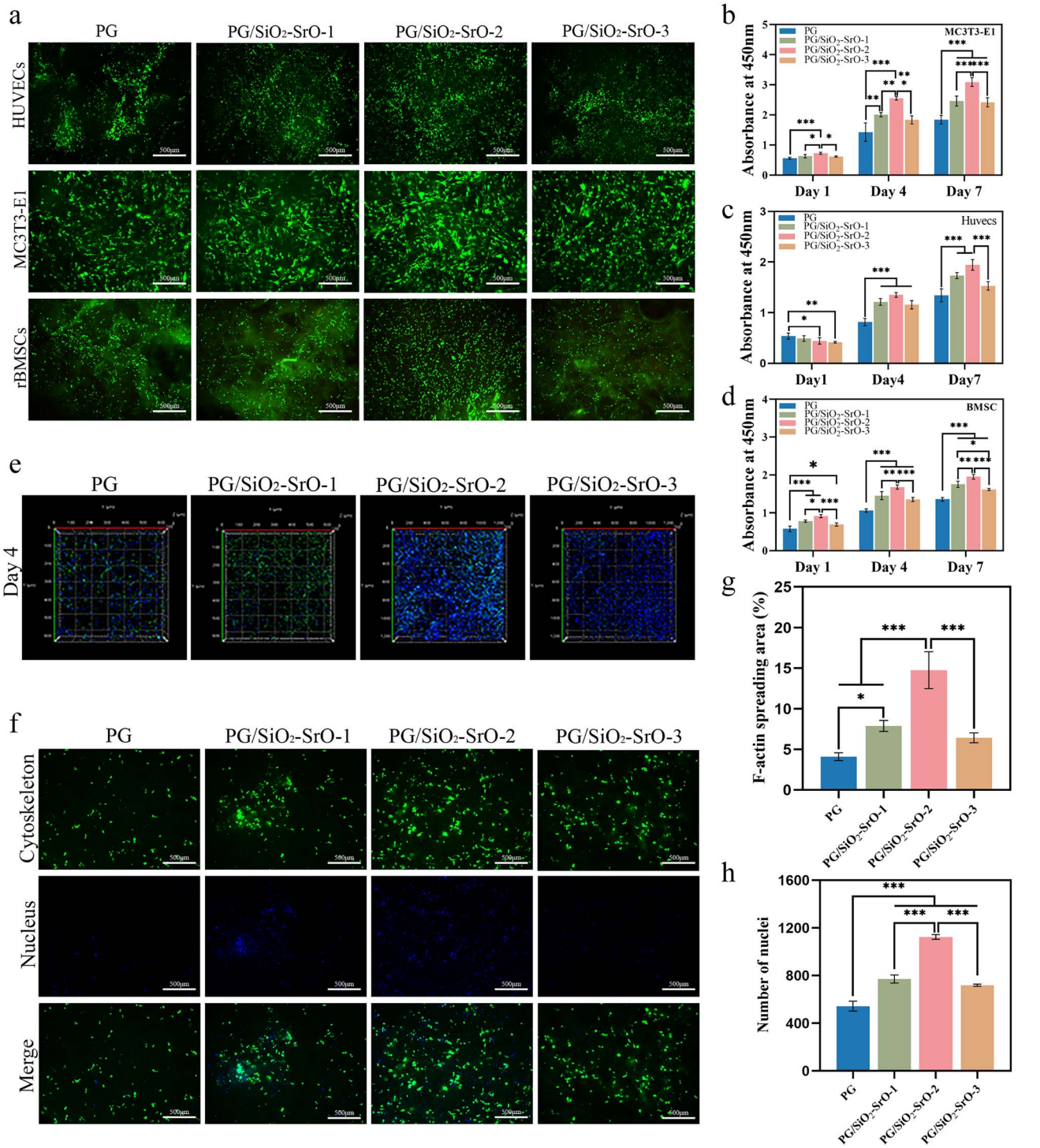

Figure 4. Cytocompatibility of scaffolds using HUVECs, MC3T3-E1, and rBMSCs. (**a**) Live/dead staining at day 7. Scar bar = 500μm. (**b-d**) Proliferation of HUVECs, MC3T3-E1, and rBMSCs cultured with different scaffolds for 1, 4, and 7 days as quantified by CCK-8 assay (n = 4). (**e**) Infiltration of MC3T3-E1 cells into scaffolds. (**f**) Cytoskeleton and nuclei staining of rBMSCs after 3 days of growth in scaffolds. Scale bar = 500 μm. (**g-h**) Cytoskeleton area and number of nuclei of rBMSCs in different types of scaffolds. n = 3. $^{*}p < 0.05$, $^{**}p < 0.01$, $^{***}p < 0.001$

Information Movie S1 demonstrates the shape recovery rate of the PG/SiO_2-SrO scaffold.

Cytocompatibility of PG/SiO_2-SrO composite aerogel scaffolds

To assess scaffold cytocompatibility, we seeded HUVECs, MC3T3-E1, and rBMSCs onto the aerogel scaffolds. Using live/dead fluorescence staining and confocal laser scanning microscopy (CLSM), we systematically analyzed cellular viability, morphological features, and penetration ability within the scaffold. Live/dead staining showed negligible cytotoxicity of scaffolds, which exhibited sufficient number of live cells, while only a few numbers of dead cells (Figure 4a). As compared to the PG scaffolds, PG/SiO_2-SrO scaffolds exhibited more number of viable cells for all cell types.

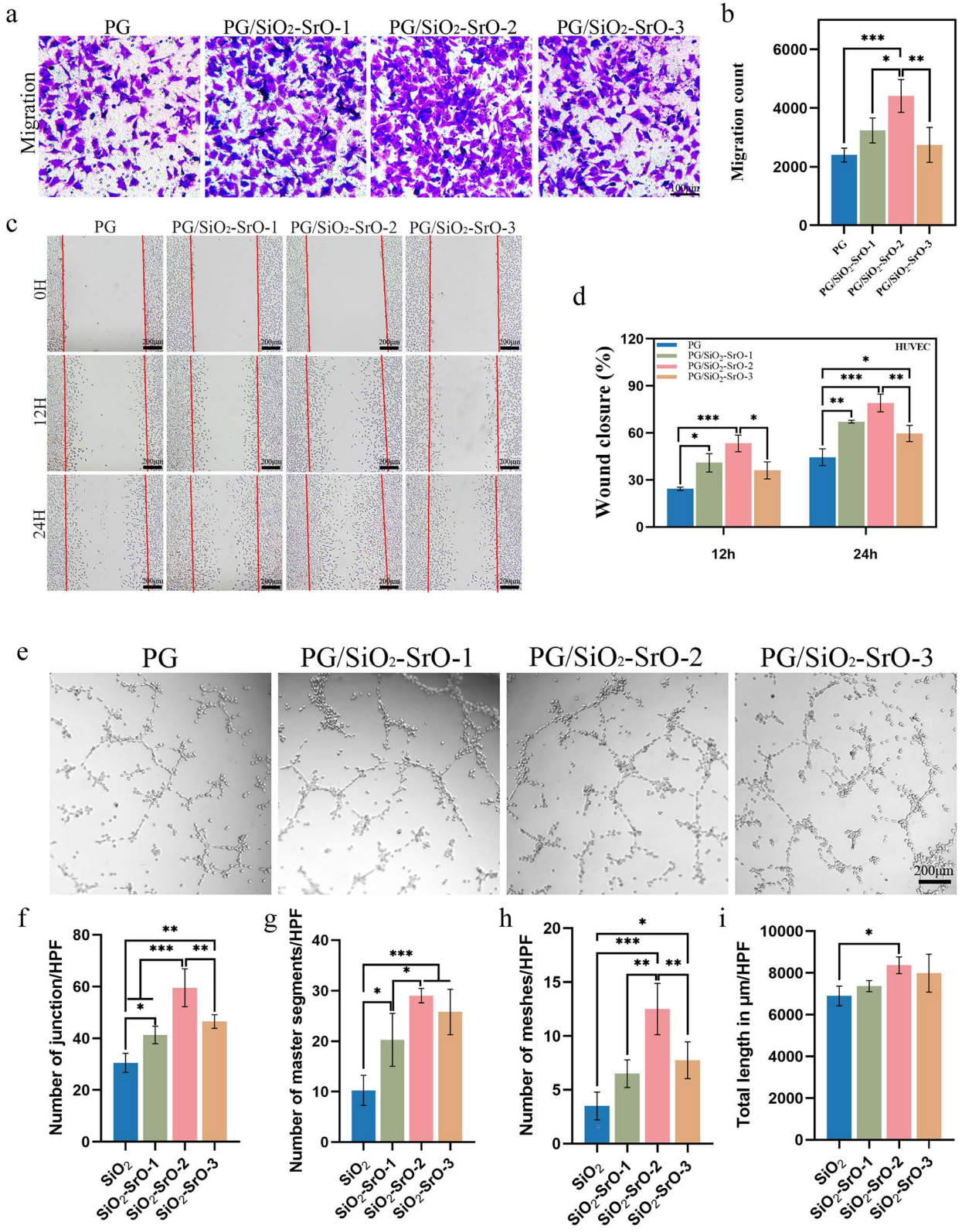

Figure 5. Cell migration and tube formation assay in vitro. (**a**) Migration of HUVECs using a Transwell assay. Scale bar = 200 μm. (**b**) Quantitative analysis of the number of the migrated cells in a Transwell migration assay. n = 4. (**c**) Scratch wound healing assay using HUVECs for up to 12 h and 24 h. HUVEC were co-cultured with extract solutions obtained from different groups. Scale bar = 100 μm. (**d**) Wound healing rate. n = 3. (**e**) Tubular networks of HUVECs co-cultured along with the conditioned media obtained from different type groups after 8 hours. Scale bar = 100 μm. (**f-i**) Quantification of junction, master segments, number of meshes and total length. n = 4. $^{*}p < 0.05$, $^{**}p < 0.01$, $^{***}p < 0.001$

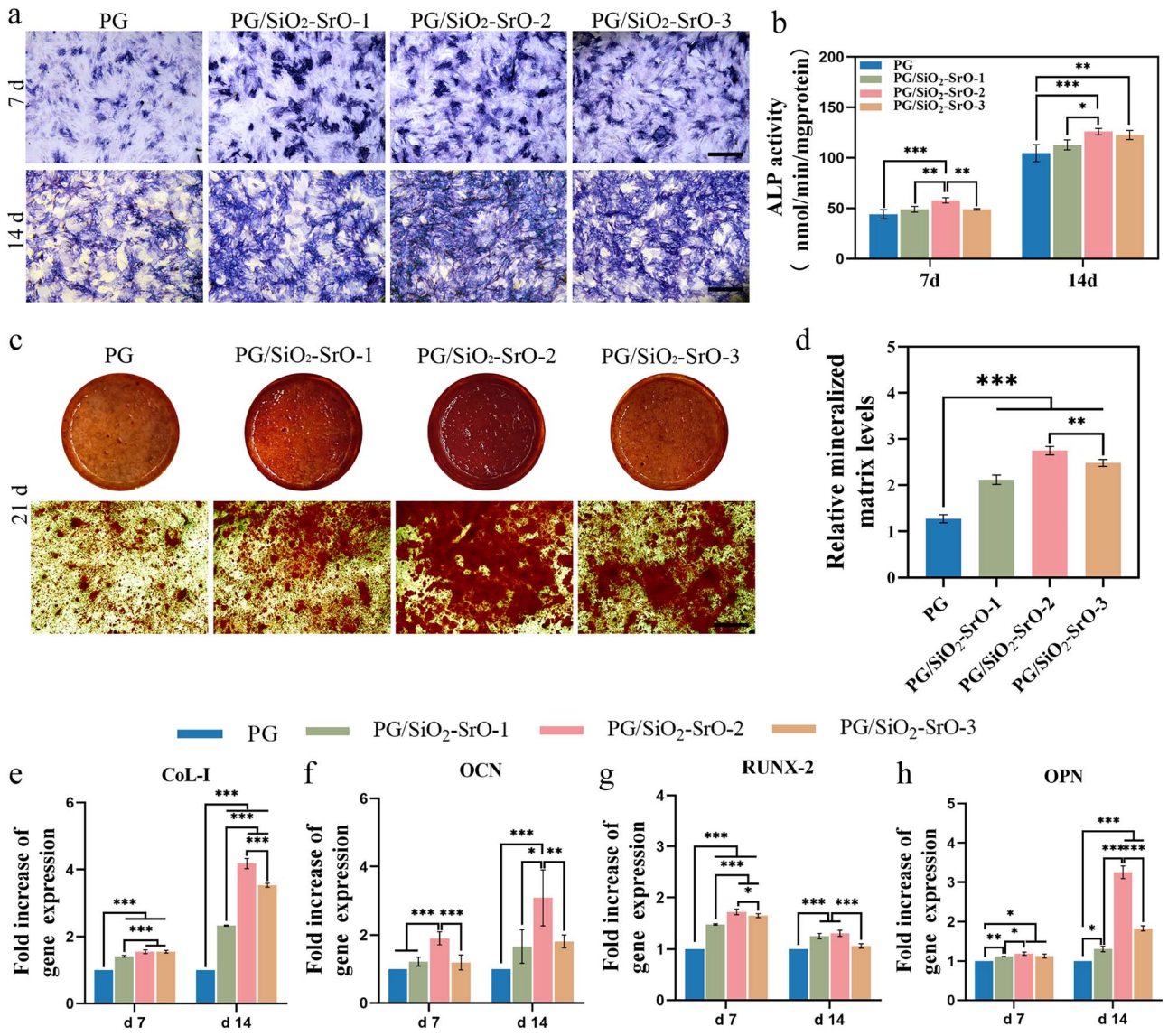

Figure 6. *In vitro* osteogenic ability of composite aerogel scaffolds. (**a**) Representative photographs of the ALP staining of BMSCs cultured along with the extract solution of different scaffold extracts at day 7 and 14 in vitro. (**b**) ALP activity at day 7 and 14 (n = 3). (**c**) ARS staining of BMSCs cultured along with the extract solution of different types of scaffolds to visualize calcium nodule formation. (**d**) Quantitative analysis of ARS staining (n = 3). (**e**-**h**) Quantification of the mRNA expression levels of COL-1, OCN, RUNX-2 and OPN genes in BMSC cultured along with the extract solution of different types of scaffolds. n = 3. $^{*}p < 0.05$, $^{**}p < 0.01$, $^{***}p < 0.001$

Especially, MC3T3-E1 cells exhibited distinct spread cell morphology, which may be attributed to the SiO_2-SrO nanofiber (Figure S3).

Bone regeneration is accompanied by mineral deposition [20]. We next elucidated the use of a simulated body fluid immersion situation to assess the mineralization of the scaffold *in vitro*. While only negligible mineral deposition had occurred as earlier as Day 3, significant mineral deposition was observed by Day 14 (Figure S3, see the spherical particles). Bionic mineralization is induced by SBF to form a Ca-phosphorus layer, which facilitates cell adhesion, migration, and osteogenic differentiation [21]. The results of CCK-8 assay was consistent with live/dead staining. The PG/SiO_2-SrO-2 group exhibited the highest cell proliferation (Figure 4b-d). Moreover, In addition, MC3T3-E1 cells had the highest infiltration rate in the PG/SiO_2-SrO-2 group of scaffolds (Figure 4e). Cytoskeletal staining by rhodamine phalloidin of the rBMSC seeded along with the scaffolds showed the highest actin cytoskeleton formation in the PG/SiO_2-SrO-2 scaffolds as compared to the other groups (Figure 4f-h).

Cellular motility and angiogenesis assay *in vitro*

To delineate the chemotactic ability of scaffolds on HUVECs, Transwell migration assay was performed. PG/SiO_2-SrO scaffold showed significant cell migration than that of the PG group. The PG/SiO_2-SrO-2 group exhibited the highest cell migration *in vitro* (Figure 5a). Quantitative analysis further showed that the PG/SiO_2-SrO-2 groups induced markedly superior cell migration rates relative to other experimental groups (Figure 5b). The scratch wound assay with HUVECs yielded concordant results with the Transwell migration data, confirming the PG/SiO_2-SrO-2 group pro-migratory effect. (Figure 5c). While all groups exhibited cell migration *in vitro*, PG/SiO_2-SrO groups outperformed other groups in terms of cell migration. The PG/SiO_2-SrO-2 group exhibited

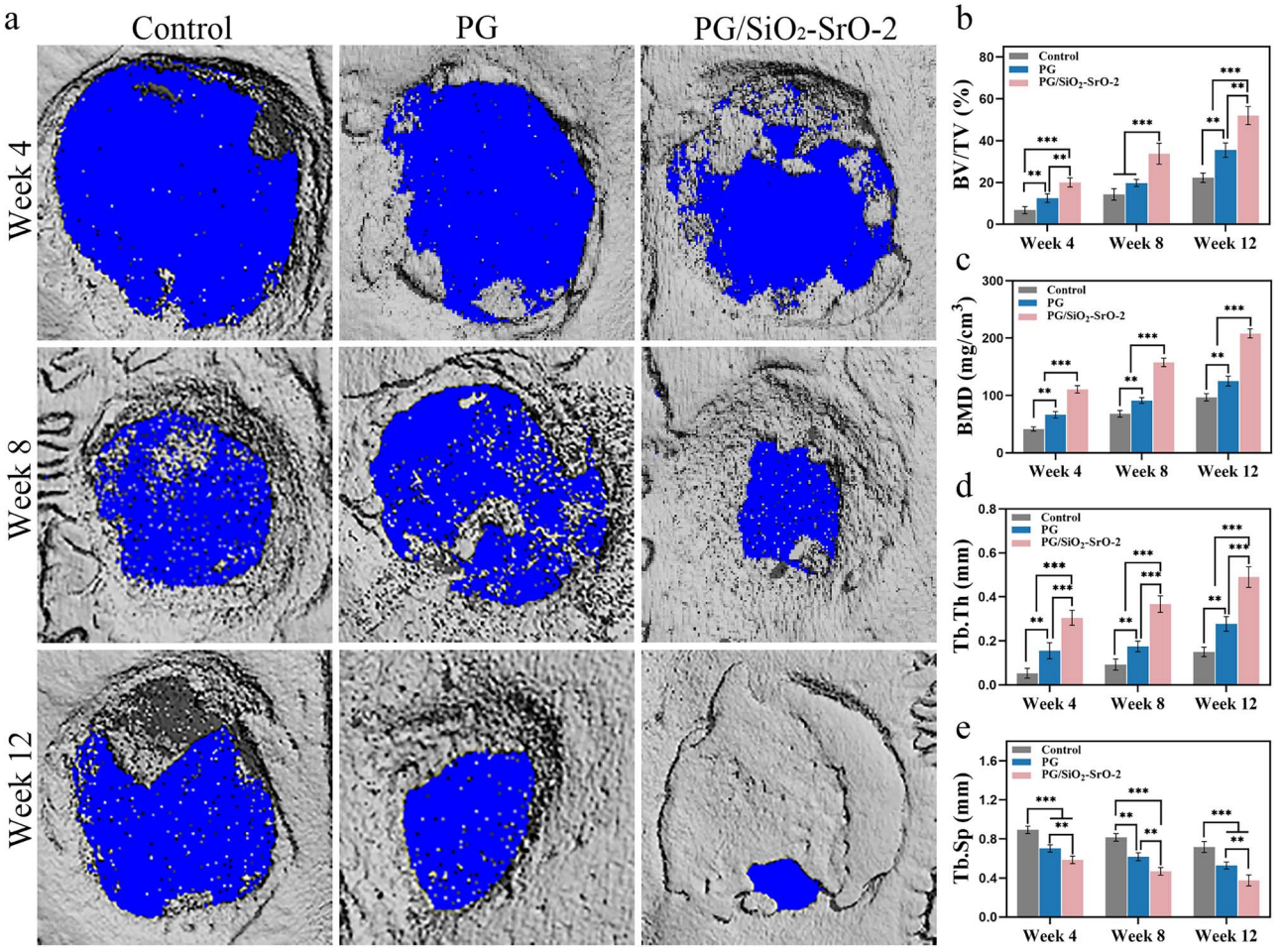

Figure 7. *In vivo* bone regeneration by scaffolds in a rat cranial defect model *in vivo*. (**a**) Representative 3D reconstructed images obtained from micro-CT scanning of the calvarial 4, 8 and 12 weeks post-implantation. (**b**) Percent object volume (BV/TV) analysis (n = 3). (**c**) Bone Mineral Density (BMD) analysis (n = 3). (**d**) Trabecular thickness (Tb.Th) analysis and (**e**) Trabecular separation (Tb.Sp) analysis. n = 3. Statistical analyses were performed by one-way analysis of variance (ANOVA) with Tukey's post hoc test , $^{*}p < 0.05$, $^{**}p < 0.01$, $^{***}p < 0.001$

rapid wound closure than that of the other aerogel groups (Figure 5d).

To further delineate the potential of scaffolds to induce angiogenesis *in vitro*, An *in vitro* angiogenesis assay was performed to evaluate HUVEC tube formation capability on Matrigel-coated plates. In the ECMatrix™ gel culture system, HUVECs showed typical angiogenic dynamics over time, with cell pseudopods developing and connecting to form mature reticular structures after 8 hours of culture (Figure 5e). The angiogenic effect of the PG/SiO_2-SrO group was significantly better than that of the PG group, which is attributed to the ability of aerogel scaffolds to furnish Si^{4+} and Sr^{2+} to promote angiogenesis [22]. PG/SiO_2-SrO-2 demonstrated superior angiogenic potential in tube formation assays compared to other experimental groups (Figure 5f-i).

Osteoinductive capacity of scaffolds under *in vitro* conditions

To discern the osteogenic ability of the scaffolds to promote the differentiation of BMSCs into osteoblasts, various assays were performed, such as ALP assay and ARS staining. Moreover, the expression of osteogenesis-related proteins at the mRNA level was studied by the RT-qPCR. The PG/SiO2-SrO scaffolds showed an intense purple color with the strongest induction of ALP activity in all tested groups (Figure 6a-b). ARS staining was further used to discern mineralization by staining Ca nodules. While all groups cultured in an osteo-inductive medium exhibited positive staining for the ARS at Day 21, PG/SiO_2-SrO-2 group displayed the highest number of Ca nodules and mineralization than that of the other groups (Figure 6c-d).

The expression of osteogenesis-related genes, including collagen type I (CoL I), OCN, RUNX2, and osteoblastin (OPN) was assessed at the mRNA level using RT-qPCR. PG and PG/SiO_2-SrO groups showed an enhanced in the expression levels of osteoblastic genes (Figure 6e-h). Notably, PG/SiO_2-SrO-2 demonstrated the most pronounced transcriptional activation, correlating well with its superior ALP activity and enhanced mineralization capacity. Taken together, these data indicated that the PG/SiO_2-SrO-2 group had distinct significantly enhances the osteogenic differentiation potential of BMSCs in terms of osteo-inductive ability and osteogenic differentiation.

Bone repair *in vivo*

The osteogenic ability of the scaffolds was also evaluated using an *in vivo* skull defect model. The new bone formation was studied by Micro-CT and histological analysis 4, 8,

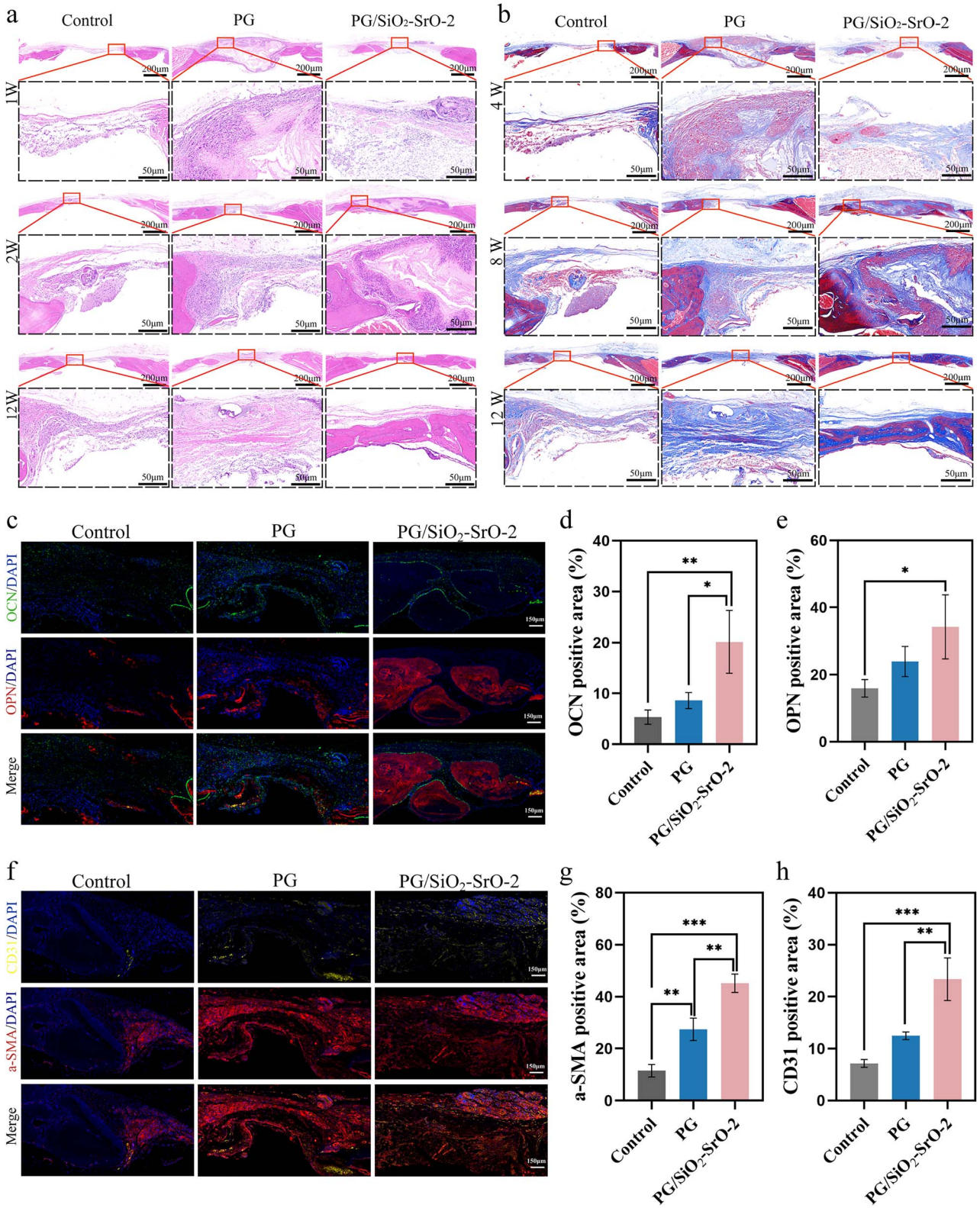

Figure 8. Histologic analysis of the defect site at different time points. (**a**) Hematoxylin and eosin (H&E) staining. (**b**) Masson's trichrome staining. (**c**) Immunofluorescence staining, including OPN (red), OCN (green), and staining of nuclei in complex with DAPI (blue). (**d**-**e**) Positive relative area results corresponding to OPN and OCN proteins, n = 3. (**f**) Immunofluorescence staining including CD31 (yellow), α-SMA (red) and nuclei stained with DAPI (blue) complex. (**g**-**h**) Positive relative area results corresponding to CD31 and α-SMA proteins, n = 3. $^{*}p < 0.05$, $^{**}p < 0.01$, $^{***}p < 0.001$

and 12 weeks post-implantation. While control group lacked significant bone formation, all experimental groups exhibited varying degrees of *de novo* bone formation. The PG/SiO_2-SrO scaffold group exhibited the highest new bone coverage at week 12 as compared to the control and PG groups and the new bone tissue filled almost an entire defect area (Figure 7a). New bone formation was quantified by bone volume fraction (BV/TV), bone mineral density, and trabecular bone thickness (Tb.Th) (Figure 7b-d) further confirmed the significant ability of the PG/SiO_2-SrO scaffolds to promote fracture healing, which is ascribed to the osteogenic and angiogenic ability of the scaffolds as well as the release of the bioactivity ions as demonstrated *in vitro* [23]. Since Sr has been previously shown to be an osteo-inductive element, SiO_2-SrO fibers may additionally act as a bridge to promote cell adhesion and proliferation, thereby enhancing the healing the bone defect.

Histological evaluation was conducted through H&E staining and Masson's trichrome staining to characterize the regenerated bone tissue (Figure 8a-b). The defect area was significantly decreased in the PG/SiO_2-SrO-2 group 12 weeks post-implantation than that of the 4 weeks post-implantation. The composite scaffolds were degraded for up to a certain level 12 weeks post-operatively with no obvious inflammatory reaction or necrosis for all groups. It is worthy to note that the defect area was filled with thin loose reticular fiber tissue with only a few number of inflammatory cells. Only a small amount of new bone was formed at the edge of the defect in the control groups. On the other hand, the PG group exhibited only a limited new bone formation, which was mainly observed at the edge of the defect. The defects treated with the PG/SiO_2-SrO-2 scaffold displayed more new bone formation spanning from the edge to the center of the defect. The new bone tissue was similar to the bone density around the defect. The PG/SiO_2-SrO-2 group showed significantly higher filling of the bone defect with the *de novo* bone. The new bone trabeculae and osteoblasts were distributed as clusters in the pores and the margins of the defect area of the scaffold, and were accompanied by a large number of capillaries. Composite scaffold groups not only showed significant *de novo* bone formation but also exhibited good osteo-integration.

In addition, Immunofluorescence analysis was additionally conducted to detect osteogenic differentiation markers osteopontin (OPN) and osteocalcin (OCN) at the protein level. The expression level of OPN and OCN was significantly higher in PG/SiO_2-SrO-2 group than that of the other groups (Figure 8c). Quantitative analysis of the OPN and OCN staining also showed the superiority of PG/SiO_2-SrO-2 scaffold over other groups (Figure 8d-e). We further ascertained angiogenesis in the defect region through CD31 and α-SMA staining. The PG/SiO_2-SrO-2 group showed significantly higher number of CD31/α-SMA-positive blood vessels than that of the control group (Figure 8f-h). Taken together, PG/SiO_2-SrO scaffold can simultaneously induce osteogenic-angiogenic induction capacity, demonstrating significant potential for bone tissue engineering applications.

Discussion

The bone is a complex organ, which is continuously remodeled according to the multi-scale biological microenvironment. The use of functional scaffolds for bone tissue engineering triggers a series of biological processes that culminate in the occurrence of bone regeneration with favorable effects. These processes stimulate cells primarily through the provision of intrinsic properties by biomaterials and/or the release of extrinsic factors. 3D scaffolds doped with therapeutic ions may leverage a conducive environment to develop robust carrier systems for the release of specific ions in bone engineering strategies. Hydroxyapatite has good biocompatibility and osteoconductivity, and is the main inorganic component of human bone, and is therefore considered to be an efficient bone tissue repair material [24]. Silicon (Si) and Sr are naturally occurring therapeutic ions. Silica (SiO_2) is a bioceramic, which can furnish therapeutic ions (e.g. Si^{4+}) and can promote bone tissue repair via enhanced osteogenic induction [25]. Strontium (Sr) can promote bone homeostasis by stimulating the differentiation of osteoblasts as well as promoting bone formation. Moreover, Sr can affect the activity of osteoclasts partly reducing osteoclast differentiation and promoting osteoclasts apoptosis, thereby promoting bone homeostasis [26, 27]. Inspired by the organic and inorganic components of the bone matrix, we proposed to construct organic–inorganic hybrid biomimetic scaffolds mimicking natural bone matrix for bone tissue repair. We prepared a 3D composite aerogel scaffold based on electrospun PG and SiO_2-SrO short fibers. *In vitro* release studies showed that the PG/SiO_2-SrO scaffold could stably and continuously release Si^{4+} and Sr^{2+} and facilitate bone tissue repair (Figure 2g-h).

The mechanical behavior of bone tissue engineering scaffolds must match native osseous tissue. An assessment of mechanical properties of scaffolds demonstrates structural integrity of the scaffold and exhibits excellent compressive properties when strained to 90% (Figure 3a). The interconnected porous network may provide a supportive 3D-like structure for cellular infiltration, and may additionally promote the organization and deposition of functional ECM and the growth of neo-vessels and other tissue-specific structures. As compared to PG scaffolds, PG/SiO_2-SrO scaffolds displayed sparse porous structure. In addition, CLSM indicated a higher propensity for the cells to migrate and proliferate towards the inner side of the PG/SiO_2-SrO scaffolds (Figure 3e).

The performance of scaffold biocompatibility is a factor that needs to be considered first and foremost in the design of scaffolds. It has been previously shown that the Si^{4+} can promote cell proliferation [28]. *In vitro* testing confirmed the pro-adhesive and proliferative effects of silicon-doped HA scaffolds [29]. Similarly, Sr has been shown stimulate both growth and osteoblastic differentiation of human bone marrow stem cells *in vitro* [30]. Si^{4+} and Sr^{2+} can also cooperative stimulation cell proliferation [31]. We observed the beneficial effect of PG/SiO_2-SrO scaffolds to promote cell growth as revealed by the live/dead staining and CCK-8 assay (Figure 4a-d). These results indicate that the scaffolds can provide a conducive microenvironment to support cell growth and metabolic activities, which may also have implications for their *in vivo* applications.

Cell migration represents a fundamental biological process that plays pivotal roles in both normal physiological functions and disease pathogenesis, including cancer metastasis, inflammation, angiogenesis, and tissue regeneration [32]. It has been previously shown that Si and Sr can promote the cell migration [33]. The scratch wound healing assay demonstrated that the PG/SiO_2-SrO-2 scaffolds have a great potential to promote cell migration in vitro, which is consistent with the conclusions of the Transwell migration assay. Since the scaffolds can

recruit cells *in vitro*, these recruited cells can help promote biomineralization and *de novo* bone tissue production.

As a highly vascularized tissue, the integrity of bone depends on angiogenesis and tight junctions of osteocytes in a spatio-temporal fashion. Adequate angiogenesis is critical in bone development and repair, so it is necessary to design available scaffolds that promote angiogenesis [34]. Si^{4+} andSr^{2+} can significantly promote the regenerative movement of vascular endothelial cells by synergistically activating the VEGF/VEGFR and PI3K/Akt signaling pathways [10, 35–37]. Compared to extracts from PG scaffolds, extracts from PG/SiO_2-SrO-2 scaffolds significantly induced the formation of angiogenic typical morphology in HUVECs, partly due to the synergistic effect of bioactive Si^{4+} and Sr^{2+}. These therapeutic ions can modulate molecular mechanisms associated with angiogenesis and can promote the migration, proliferation and differentiation of ECs. Consequently, PG/SiO_2-Sr-2 scaffolds may have considerable prospect for the regeneration of vascularized bone tissue.

The expression level of ALP can be used as a marker to assess the differentiation status and metabolic activity of osteoblasts. Silicon ions (Si^{4+}) have been shown to promote the ALP expression as well as promote the differentiation of osteoblasts [29]. PG/SiO_2-SrO scaffold exhibited significantly higher ALP expression than that of the PG scaffolds (Figure 6a-b). Another aspect, Sr activates the differentiation of MSCs to osteoblasts by up-regulating the expression of RUNX2 [38]. The PG/SiO_2-SrO scaffolds also significantly enhanced the transcriptional activity of key osteogenic markers, such as COL 1, OCN, RUNX2, and OPN, which is indicative of the osteo-inductive ability of scaffolds (Figure 6e-h).

The osteogenic effects of Si^{4+} are mediated through upregulation of Wnt/β-catenin cascade [39]. Axis inhibitor protein 2 (AXIN2) is a signal transducer of the Wnt signaling pathway. β-catenin promotes cell proliferation and differentiation as a central mediator of Wnt/β-catenin signaling. It has been shown that Si^{4+} can significantly upregulate the gene expression of AXIN2 and β-catenin [40]. Similarly, Sr^{2+} can promote the expression of frizzled 8 (FZD8) and β-catenin, thereby further activating different types of transcription factors (e.g. RUNX2). Moreover, Sr^{2+} can inhibit Wnt signaling via the down-regulation of protein phosphatase 2A; the later can prevent the degradation of β-catenin and promote osteogenic differentiation of MSCs [41]. Therefore, the combined delivery of Si^{4+} and Sr^{2+} can enhance the activity of the classical Wnt/β-catenin pathway through the modulation of the extracellular signal-regulated kinase/mediator-activated protein kinase (ERK/MAPK) signaling pathway, and coupled to promote the osteogenesis process of composite scaffolds. [42–45].

We further evaluated the beneficial effects of PG/SiO_2-SrO scaffolds in promoting neogenesis in a rat skull defect model (Figure 7a). PG/SiO_2-SrO scaffold showed the ingrowth of *de novo* bone tissues both at the outer as well as inner sides of the scaffolds. Moreover, the new bone tissues were well integrated with the scaffold, thereby promoting bone tissue repair. Histological analysis and immunohistochemical staining showed the beneficial effect of PG/SiO_2-SrO scaffold were optimal in promoting bone tissue repair (Figure 8a-h).

Taken together, we successfully fabricated a 3D composite aerogel scaffold based on SiO_2-SrO short fibers and PG fibers. The scaffold not only displayed cytocompatibility and biocompatibility concomitant with sufficient biomechanical characteristics for bone tissue repair, but they also afforded the sustained and controlled release of therapeutic ions, such as Si^{4+} and Sr^{2+}. These functional ions can synergistically act to promote osteogenic differentiation of MSC and biomineralization. Moreover, these therapeutic ions can synergistically activate osteogenic and angiogenic mechanisms, thereby enhancing the efficiency of bone regeneration.

Conclusions

In summary, we have successfully developed composite aerogel scaffolds based on flexible SiO_2-SrO short nanofibers and PG fibers (PG/SiO_2-SrO), which closely mimiced the mixture components of natural bone tissue. PG/SiO_2-SrO scaffolds exhibited excellent good physical and chemical properties, released Si^{4+} and Sr^{2+}, as well as promoted cellular behaviors, and osteogenic differentiation of rBMSC. PG/SiO_2-SrO-2 scaffold group exhibited higher *de novo* bone production in a skull defect model in rats as observed for up to 12 weeks. In summary, we simultaneously utilize PLA/Gel and SiO_2-SrO fibers to afford composite aerogel scaffolds may have broad implications to impart multifunctional characteristics to the scaffolds for bone defect repair and related biomedical fields.

Author contributions

Jie Cui (Conceptualization [equal], Data curation [equal], Formal analysis [equal], Investigation [equal], Methodology [equal], Writing—original draft [equal]), Lixiang Zhang (Formal analysis [equal]), Muhammad Shafiq (Formal analysis [supporting], Methodology [supporting], Writing—original draft [equal], Writing—review & editing [equal]), Panpan Shang (Resources [equal]), Xiao Yu (Formal analysis [equal]), Yangfan Ding (Formal analysis [equal]), Pengfei Cai (Formal analysis [equal]), Jiahui Song (Formal analysis [equal]), Binbin Sun (Resources [equal]), Mohamed EL-Newehy (Formal analysis [equal]), Meera Moydeen Abdulhameed (Formal analysis [equal]), Stachewicz Urszula (Software [equal]), Xingping Zhou (Supervision [equal]), yuan xu (Funding acquisition [equal], Methodology [equal], Resources [equal], Supervision [equal]), Xiumei Mo (Funding acquisition [equal], Resources [equal], Supervision [equal], Writing—review & editing [equal]).

Supplementary data

Supplementary data are available at *Burns & Trauma Journal* online.

Funding

This project was supported by the Fundamental Research Funds for the Central Universities (CUSF-DH-T-2023064), the Fundamental Research Funds for the Central Universities (2232023D-10), Science and Technology Commission of Shanghai Municipality, China (20DZ2254900), Sino German Science Foundation Research Exchange Center, China (M-0263), and China Education Association for International Exchange (2022181). This project was also supported by Ongoing Research Funding program (ORF-2025-769), King Saud University, Riyadh, Saudi Arabia. This project was also supported by the Science and Technology Research Program of Chongqing Municipal Education Commission (KJZD-K202412807), Youth Doctoral Talent Incubation Program of the Second Affiliated Hospital, Army Medical

University (2023YQB002). This project was also supported by the Chenguang Program of Shanghai Education Development Foundation and Shanghai Municipal Education Commission (23CGB08).

Conflict of interest statement

None declared.

References

1. Xue N, Ding X, Huang R, Jiang R, Huang H, Pan X. *et al.* Bone tissue engineering in the treatment of bone defects. *Pharmaceuticals (Basel)* 2022;**15**:15. https://doi.org/10.3390/ph15070879.
2. Campana V, Milano G, Pagano E, Barba M, Cicione C, Salonna G. *et al.* Bone substitutes in orthopaedic surgery: from basic science to clinical practice. *J Mater Sci Mater Med* 2014;**25**:2445–61. https://doi.org/10.1007/s10856-014-5240-2.
3. Schlickewei W, Schlickewei C. The use of bone substitutes in the treatment of bone defects – the clinical view and history. *Macromol Symp* 2007;**253**:10–23. https://doi.org/10.1002/masy.200750702.
4. Ma J, Wu S, Liu J, Liu C, Ni S, Dai T. *et al.* Synergistic effects of nanoattapulgite and hydroxyapatite on vascularization and bone formation in a rabbit tibia bone defect model. *Biomaterials Science* 2022;**10**:4635–55. https://doi.org/10.1039/D2BM00547F.
5. Tobeiha M, Moghadasian M H, Amin N, Jafarnejad S, Deligianni D. Rankl/rank/opg pathway: A mechanism involved in exercise-induced bone remodeling, *BioMed Research International* 2020;**6910312**;**11**:6910312. https://doi.org/10.1155/2020/6910312.
6. Amjadi-Moheb F, Akhavan-Niaki H. Wnt signaling pathway in osteoporosis: epigenetic regulation, interaction with other signaling pathways, and therapeutic promises. *J Cell Physiol* 2019;**234**:14641–50. https://doi.org/10.1002/jcp.28207.
7. Gao Y, Chen N, Fu Z, Zhang Q. Progress of wnt signaling pathway in osteoporosis. *Biomol Ther* 2023;**13**:13. https://doi.org/10.3390/biom13030483.
8. Pritchard A, Nielsen BD. Silicon supplementation for bone health: an umbrella review attempting to translate from animals to humans. *Nutrients* 2024;**16**:339. https://doi.org/10.3390/nu16030339.
9. Rondanelli M, Faliva MA, Peroni G, Gasparri C, Perna S, Riva A. *et al.* Silicon: a neglected micronutrient essential for bone health. *Exp Biol Med* 2021;**246**:1500–11. https://doi.org/10.1177/1535370221997072.
10. Wang X, Gao L, Han Y, Xing M, Zhao C, Peng J. *et al.* Silicon-enhanced adipogenesis and angiogenesis for vascularized adipose tissue engineering. *Adv Sci* 2018;**5**:1800776.
11. Zheng Y, Wang J, Zhao T, Wang L, Wang J. Modulation of the vegf/akt/enos signaling pathway to regulate liver angiogenesis to explore the anti-hepatic fibrosis mechanism of curcumol. *J Ethnopharmacol* 2021;**280**:114480. https://doi.org/10.1016/j.jep.2021.114480.
12. Seo SH, Hwang SY, Hwang S, Han S, Park H, Lee YS. *et al.* Hypoxia-induced elf3 promotes tumor angiogenesis through igf1/igf1r. *EMBO Rep* 2022;**23**:e52977. https://doi.org/10.15252/embr.202152977.
13. Zhu Y, Shen Y, Xiang Y, Fang K, Xu K, Ma P. *et al.* Combined application of silica particles and zirconium hydrogen phosphate coating to improve the friction resistance and osteogenic/anti-inflammatory properties of micro-arc oxidation-treated titanium. *Surf Coat Technol* 2022;**451**:129037. https://doi.org/10.1016/j.surfcoat.2022.129037.
14. Iglesias-Mejuto A, Magariños B, Ferreira-Gonçalves T, Starbird-Pérez R, Álvarez-Lorenzo C, Reis CP. *et al.* Vancomycin-loaded methylcellulose aerogel scaffolds for advanced bone tissue engineering. *Carbohydr Polym* 2024;**324**:121536. https://doi.org/10.1016/j.carbpol.2023.121536.
15. Reyes-Peces MV, Pérez-Moreno A, De-Los-Santos DM, Mesa-Díaz MDM, Pinaglia-Tobaruela G, Vilches-Pérez JI. *et al.* Chitosan-gptms-silica hybrid mesoporous aerogels for bone tissue engineering. *Polymers* 2020;**12**:12. https://doi.org/10.3390/polym12112723.
16. El-Wakil N, Kamel R, Mahmoud AA, Dufresne A, Abouzeid RE, Abo El-Fadl Mahmoud T. *et al.* Risedronate-loaded aerogel scaffolds for bone regeneration. *Drug Delivery* 2022;**30**:51–63. https://doi.org/10.1080/10717544.2022.2152135.
17. Li Z, Li S, Yang J, Ha Y, Zhang Q, Zhou X. *et al.* 3d bioprinted gelatin/gellan gum-based scaffold with double-crosslinking network for vascularized bone regeneration. *Carbohydr Polym* 2022;**290**:119469. https://doi.org/10.1016/j.carbpol.2022.119469.
18. Liu M, Shafiq M, Sun B, Wu J, Wang W, El-Newehy M. *et al.* Composite superelastic aerogel scaffolds containing flexible Sio_2 nanofibers promote bone regeneration. *Advanced Healthcare Materials* 2022;**11**:11. https://doi.org/10.1002/adhm.202200499.
19. Qiao Y, Yu L, Yang P, Chen M, Sun H, Wang L. *et al.* Spatiotemporal immunomodulation and biphasic osteo-vascular aligned electrospun membrane for diabetic periosteum regeneration, advanced. *Science* 2023;**10**:10. https://doi.org/10.1002/advs.202302874.
20. Li C, Xu W, Li L, Zhou Y, Yao G, Chen G. *et al.* Concrete-inspired bionic bone glue repairs osteoporotic bone defects by gluing and remodeling aging macrophages, advanced. *Science* 2024;**11**:11. https://doi.org/10.1002/advs.202408044.
21. Yang L, Li W, Ding X, Zhao Y, Qian X, Shang L. Biomimetic mineralized organic–inorganic hybrid scaffolds from microfluidic 3d printing for bone repair. *Adv Funct Mater* 2024;**35**:2410927. https://doi.org/10.1002/adfm.202410927.
22. Lin K, Xia L, Li H, Jiang X, Pan H, Xu Y. *et al.* Enhanced osteoporotic bone regeneration by strontium-substituted calcium silicate bioactive ceramics. *Biomaterials* 2013;**34**:10028–42. https://doi.org/10.1016/j.biomaterials.2013.09.056.
23. Wu Q, Xu S, Wang X, Jia B, Han Y, Zhuang Y. *et al.* Complementary and synergistic effects on osteogenic and angiogenic properties of copper-incorporated silicocarnotite bioceramic: In vitro and in vivo studies. *Biomaterials* 2021;**268**:120553. https://doi.org/10.1016/j.biomaterials.2020.120553.
24. Huang G-J, Yu H-P, Wang X-L, Ning B-B, Gao J, Shi Y-Q. *et al.* Highly porous and elastic aerogel based on ultralong hydroxyapatite nanowires for high-performance bone regeneration and neovascularization. *J Mater Chem B* 2021;**9**:1277–87. https://doi.org/10.1039/D0TB02288H.
25. Alvarez Echazú M, Renou S, Alvarez G, Desimone M, Olmedo D. A collagen-silica-based biocomposite for potential application in bone tissue engineering. *J Biomed Mater Res A* 2021;**110**:331–40. https://doi.org/10.1002/jbm.a.37291.
26. Lei Y, Xu Z, Ke Q, Yin W, Chen Y, Zhang C. *et al.* Strontium hydroxyapatite/chitosan nanohybrid scaffolds with enhanced osteoinductivity for bone tissue engineering. *Mater Sci Eng C* 2017;**72**:134–42. https://doi.org/10.1016/j.msec.2016.11.063.
27. Boda SK, Thrivikraman G, Panigrahy B, Sarma DD, Basu B. Competing roles of substrate composition, microstructure, and sustained strontium release in directing osteogenic differentiation of hmscs. *ACS Appl Mater Interfaces* 2016;**9**:19389–408. https://doi.org/10.1021/acsami.6b08694.
28. Shie M-Y, Ding S-J, Chang H-C. The role of silicon in osteoblast-like cell proliferation and apoptosis. *Acta Biomater* 2011;**7**:2604–14. https://doi.org/10.1016/j.actbio.2011.02.023.
29. Sun T, Wang M, Shao Y, Wang L, Zhu Y. The effect and osteoblast signaling response of trace silicon doping hydroxyapatite. *Biol Trace Elem Res* 2017;**181**:82–94. https://doi.org/10.1007/s12011-017-1031-1.
30. Kruppke B, Heinemann C, Wagner AS, Farack J, Wenisch S, Wiesmann HP. *et al.* Strontium ions promote in vitro human bone marrow stromal cell proliferation and differentiation in

calcium-lacking media. *Develop Growth Differ* 2018;**61**:166–75. https://doi.org/10.1111/dgd.12588.
31. Xing M, Wang X, Wang E, Gao L, Chang J. Bone tissue engineering strategy based on the synergistic effects of silicon and strontium ions. *Acta Biomater* 2018;**72**:381–95. https://doi.org/10.1016/j.actbio.2018.03.051.
32. Yang D, Zhao Z, Bai F, Wang S, Tomsia AP, Bai H. Promoting cell migration in tissue engineering scaffolds with graded channels. *Advanced Healthcare Materials* 2017;**6**:1700472. https://doi.org/10.1002/adhm.201700472.
33. Awad K, Ahuja N, Fiedler M, Peper S, Wang Z, Aswath P. *et al.* Ionic silicon protects oxidative damage and promotes skeletal muscle cell regeneration. *Int J Mol Sci* 2021;**22**:497. https://doi.org/10.3390/ijms22020497.
34. Huang J, Han Q, Cai M, Zhu J, Li L, Yu L. *et al.* Effect of angiogenesis in bone tissue engineering. *Ann Biomed Eng* 2022;**50**:898–913. https://doi.org/10.1007/s10439-022-02970-9.
35. Zhuang Y, Liu A, Jiang S, Liaqat U, Lin K, Sun W. *et al.* Promoting vascularized bone regeneration via strontium-incorporated hydroxyapatite bioceramic. *Mater Des* 2023;**234**:112313. https://doi.org/10.1016/j.matdes.2023.112313.
36. Wang L, Shen M, Tang Z, Tan J, Li K, Ma H. 3d printed magnesium silicate/β-tricalcium phosphate scaffolds promote coupled osteogenesis and angiogenesis. *Frontiers in Bioengineering and Biotechnology* 2025;**12**:12. https://doi.org/10.3389/fbioe.2024.1518145.
37. Ma J, Qin C, Wu J, Zhang H, Zhuang H, Zhang M. *et al.* 3d printing of strontium silicate microcylinder-containing multicellular biomaterial inks for vascularized skin regeneration. *Advanced Healthcare Materials* 2021;**10**:10. https://doi.org/10.1002/adhm.202100523.
38. Kołodziejska B, Stępień N, Kolmas J. The influence of strontium on bone tissue metabolism and its application in osteoporosis treatment. *Int J Mol Sci* 2021;**22**:22. https://doi.org/10.3390/ijms22126564.
39. Zhang W, Huang D, Zhao F, Gao W, Sun L, Li X. *et al.* Synergistic effect of strontium and silicon in strontium-substituted sub-micron bioactive glass for enhanced osteogenesis. *Mater Sci Eng C* 2018;**89**:245–55. https://doi.org/10.1016/j.msec.2018.04.012.
40. Han P, Wu C, Xiao Y. The effect of silicate ions on proliferation, osteogenic differentiation and cell signalling pathways (wnt and shh) of bone marrow stromal cells. *Biomater Sci* 2013;**1**:379–92. https://doi.org/10.1039/C2BM00108J.
41. Yang F, Yang D, Tu J, Zheng Q, Cai L, Wang L. Strontium enhances osteogenic differentiation of mesenchymal stem cells and in vivo bone formation by activating wnt/catenin signaling. *Stem Cells* 2011;**29**:981–91. https://doi.org/10.1002/stem.646.
42. Wu Q, Hu L, Yan R, Shi J, Gu H, Deng Y. *et al.* Strontium-incorporated bioceramic scaffolds for enhanced osteoporosis bone regeneration. *Bone Res* 2022;**10**:55. https://doi.org/10.1038/s41413-022-00224-x.
43. Yu X, Shen Y, Cui J, Ding Y, Morsi Y, Sun B. *et al.* The potential application of electrical stimulation in tendon repair: a review. *Med-X* 2025;**3**:3. https://doi.org/10.1007/s44258-025-00051-9.
44. Bosch-Rué E, Diez-Tercero L, Giordano-Kelhoffer B, Delgado LM, Bosch BM, Hoyos-Nogués M. *et al.* Biological roles and delivery strategies for ions to promote osteogenic induction. *Frontiers in Cell and Developmental Biology* 2021;8.
45. Cheng D, Ding R, Jin X, Lu Y, Bao W, Zhao Y. *et al.* Strontium ion-functionalized nano-hydroxyapatite/chitosan composite microspheres promote osteogenesis and angiogenesis for bone regeneration. *ACS Appl Mater Interfaces* 2023;**15**:19951–65. https://doi.org/10.1021/acsami.3c00655.

Burns & Trauma, 2025, 13, tkaf028
https://doi.org/10.1093/burnst/tkaf028
Research Article